

Bivariate DeepKriging for Large-scale Spatial Interpolation of Wind Fields

Pratik Nag*

Ying Sun

CEMSE Division, Statistics Program,
King Abdullah University of Science and Technology, Saudi Arabia.

and

Brian J Reich

Department of Statistics,
North Carolina State University, Raleigh, USA.

September 27, 2024

Abstract

High spatial resolution wind data play a crucial role in various fields such as climate, oceanography, and meteorology. However, spatial interpolation or downscaling of bivariate wind fields, characterized by velocity in two dimensions, poses a challenge due to their non-Gaussian nature, high spatial variability, and heterogeneity. While cokriging is commonly employed in spatial statistics for predicting bivariate spatial fields, it is suboptimal for non-Gaussian processes and computationally prohibitive for large datasets. In this paper, we introduce bivariate DeepKriging, a novel method utilizing a spatially dependent deep neural network (DNN) with an embedding layer constructed by spatial radial basis functions for predicting bivariate spatial data. Additionally, we devise a distribution-free uncertainty quantification technique based on bootstrap and ensemble DNN. We establish the theoretical basis for bivariate DeepKriging by linking it with the Linear Model of Coregionalization (LMC). Our proposed approach surpasses traditional cokriging predictors, including those utilizing commonly used covariance functions like the linear model of co-regionalization and parsimonious bivariate Matérn covariance. We demonstrate the computational efficiency and scalability of the proposed DNN model, achieving computation speeds approximately 20 times faster than conventional techniques. Furthermore, we apply the bivariate DeepKriging method to wind data across the Middle East region at 506,771 locations, showcasing superior prediction performance over cokriging predictors while significantly reducing computation time.

*The authors gratefully acknowledge KAUST for funding this research.

Keywords: Bivariate spatial modelling, Deep learning, Feature embedding, Probabilistic prediction, Radial basis function, Spatial regression

1 Introduction

Cokriging ([Goovaerts, 1998](#)), a multivariate extension of univariate kriging, is widely used for analysis and prediction of multivariate spatial fields in multivariate spatial statistics. Prediction (with uncertainty quantification) at new unobserved sites using the information gained from the observed locations is one of the common objectives of this strategy. For Gaussian random fields with known covariance structure, cokriging is the best linear unbiased predictor. However, in reality, this requirement of Gaussianity and properly stated covariance is rarely met. Because of this, modeling heavy-tailed or skewed data with complicated covariance structure requires a more adaptable prediction methodology.

Various approaches have been proposed to model non-Gaussian spatial data such as scale mixing Gaussian random fields ([Fonseca and Steel, 2011](#)), multiple indicator kriging ([Journal and Alabert, 1989](#)), skew-Gaussian processes ([Zhang and El-Shaarawi, 2010](#)), copula-based multiple indicator kriging ([Agarwal et al., 2021](#)) and Bayesian nonparametrics ([Reich and Fuentes, 2015](#)). To address the nonstationary behaviour of the random fields over a large region, non-stationary Matérn covariance models ([Nychka et al., 2002](#); [Paciorek and Schervish, 2003](#); [Cressie and Huang, 1999](#); [Fuentes, 2001](#)) have been introduced. Trans-Gaussian random fields ([Cressie, 1993](#); [De Oliveira et al., 2002](#)) find nonlinear transformations which enables application of Gaussian processes on the transformed data. However, marginal transformation to normality may not confirm joint normality at multiple locations and may change important properties of the variable ([Changyong et al., 2014](#)). One common drawback of many of the approaches is that there is no straight forward implementation of these methods in the bivariate setting and also they may not be

optimal for more general spatial datasets. Another issue is that most of these models are based on Gaussian processes which uses cholesky decomposition of the $N \times N$ covariance matrix which requires $\mathcal{O}(N^3)$ time and $\mathcal{O}(N^2)$ memory complexity where N is the number of spatial locations.

Recently, Deep neural network (DNN) based algorithms have proved to be the most powerful prediction methodologies in the field of computer vision and natural language processing (LeCun et al., 2015). DNNs can handle more complex functions and in theory they can be applied to approximate any function which is appealing for modelling large-scale nonstationary and non-Gaussian spatial processes. DNNs are also computationally efficient and thus can be applied to large datasets. The computation time for training can be massively reduced by using GPUs (Najafabadi et al., 2015). Due to this broad applicability of the neural networks, several researchers are trying to incorporate DNNs in the spatial problems (Wikle and Zammit-Mangion, 2022). Cracknell and Reading (2014) included spatial coordinates as features for DNNs. Wang et al. (2019) proposed a nearest neighbour neural network approach for Geostatistical modelling. Zammit-Mangion et al. (2021) used neural networks to estimate the warping function which transforms the spatial domain to fit stationary and isotropic covariance structure. Convolutional neural networks (CNNs) (Krizhevsky et al., 2012) can capture the spatial dependence successfully, but require a huge amount of data on regular grid for model training. However, in environmental statistics scenarios one of the main objective is to give spatial interpolation at unobserved locations for irregular grid datasets which is infeasible for CNN modelling. Most of these DNN based methods are developed for univariate data and only concentrate on point predictions

and ignore the prediction interval estimations. Recently, there has been few works which proposes density function estimation of the predictive distribution using neural networks, for example [Li et al. \(2019\)](#) proposed a discretized density function approach and predict the predictive distribution probabilities by training a neural network classifier. [Neal \(2012\)](#) and [Posch et al. \(2019\)](#) applied Bayesian inference methodologies to neural networks to predict uncertainties via posterior distributions. But none of these methods are directly applicable to spatial applications.

To address these drawbacks [Chen et al. \(2022\)](#) introduced a spatially dependent deep neural network structure called DeepKriging, for univariate spatial prediction. They used basis functions to capture spatial dependence and use them as features to fit the model. They also provided an approach for uncertainty quantification by an histogram based approach. However, the histograms require thresholds which are mostly deterministic and choice of the thresholds effects the results drastically.

The objective of this study is to establish a nonparametric statistical framework for conducting bivariate spatial prediction and estimating prediction uncertainties. Our proposed approach, a bivariate extension of DeepKriging (**Biv.DeepKriging**), aims to address these limitations. We introduce a spatially dependent neural network by incorporating an embedding layer of spatial coordinates using basis functions. Additionally, we propose a bootstrap and ensemble neural network-based prediction interval for prediction uncertainty. **Biv.DeepKriging** is non-parametric, making it more versatile and applicable to non-Gaussian, nonstationary, and even categorical prediction problems. Through simulations, we demonstrate that this approach yields comparable results to cokriging when the

underlying process is Gaussian, and it surpasses traditional statistical methodologies in non-Gaussian and nonstationary scenarios. Moreover, our proposed approach significantly reduces computation time compared to traditional methods.

While architecturally **Biv.DeepKriging** is a straightforward extension of univariate DeepKriging, integrating this methodology with traditional statistical methods remains a challenging task. In this paper, we illustrate that under certain conditions, the linear model of coregionalization (LMC) represents a special case of **Biv.DeepKriging**. Additionally, we introduce a novel methodology for computing prediction intervals using bootstrap and ensemble neural networks. Additionally, the execution of **Biv.DeepKriging** is computationally twenty times faster than traditional statistical approaches, effectively overcoming the bottleneck associated with applying this method to large datasets.

The remainder of our paper is structured as follows. Section 2 outlines the proposed methodology. Section 3 compares the performance of the proposed method with traditional approaches. Lastly, Section 4 applies the **Biv.DeepKriging** method to Saudi Arabian wind data. More detailed information on the exploratory data analysis of the wind dataset and further results on simulation studies can be found in the Supplementary materials.

2 Bivariate DeepKriging

2.1 Background

Let $\{\mathbf{Y}(\mathbf{s}) = \{Y_1(\mathbf{s}), Y_2(\mathbf{s})\}^T, s \in D\}$, $D \subseteq \mathbb{R}^p$, be a bivariate spatial process, and $\{\mathbf{Z}(\mathbf{s}_1), \mathbf{Z}(\mathbf{s}_2), \dots, \mathbf{Z}(\mathbf{s}_N)\}$ be the realization of the process at N spatial locations, where $\mathbf{Z}(\mathbf{s}) =$

$\{Z_1(\mathbf{s}), Z_2(\mathbf{s})\}^T$.

A classical spatial model assumes

$$\mathbf{Z}(\mathbf{s}) = \mathbf{Y}(\mathbf{s}) + \boldsymbol{\epsilon}(\mathbf{s}) \quad (1)$$

where $\boldsymbol{\epsilon}(\mathbf{s}) = \{\epsilon_1(\mathbf{s}), \epsilon_2(\mathbf{s})\}^T$, known as the nugget effect, is a bivariate white noise process with variances $\sigma_1^2(\mathbf{s})$ and $\sigma_2^2(\mathbf{s})$, respectively.

Given observations $\mathbf{Z}(\mathbf{s})$, one of the main objectives of spatial prediction is to find the best predictor of the true process $\mathbf{Y}(\mathbf{s}_0)$ at the unobserved location \mathbf{s}_0 . The optimal predictor with parameter set $\boldsymbol{\theta}$ can be defined by minimizing the expected value of the loss function, that is,

$$\hat{\mathbf{Y}}^{opt}(\mathbf{s}_0|\mathbf{Z}_N) = \mathbb{E}\{L(\hat{\mathbf{Y}}(\mathbf{s}_0), \mathbf{Y}(\mathbf{s}_0))|\mathbf{Z}_N\} = \underset{\hat{\mathbf{Y}}}{\operatorname{argmin}} R(\hat{\mathbf{Y}}(\mathbf{s}_0)|\mathbf{Z}_N),$$

where $\hat{\mathbf{Y}}^{opt}(\mathbf{s}_0|\mathbf{Z}_N)$ is the optimal predictor given $\mathbf{Z}_N = \{\mathbf{Z}(\mathbf{s}_1), \mathbf{Z}(\mathbf{s}_2), \dots, \mathbf{Z}(\mathbf{s}_N)\}$. The function $R(\cdot)$ is the risk function, which is the approximation of the loss L .

Bivariate kriging, also known as Cokriging, is the best linear unbiased predictor ([Stein and Corsten, 1991](#); [Goovaerts, 1998](#)) for bivariate spatial prediction. The spatial process $\mathbf{Y}(\mathbf{s})$ is typically modeled as

$$\mathbf{Y}(\mathbf{s}) = \boldsymbol{\mu}(\mathbf{s}) + \boldsymbol{\gamma}(\mathbf{s}),$$

where $\boldsymbol{\gamma}(\mathbf{s}) = \{\gamma_1(\mathbf{s}), \gamma_2(\mathbf{s})\}$ is a spatially-dependent zero-mean bivariate random process with cross-covariance function $\mathbf{C}_{u,v}(\mathbf{s}_i, \mathbf{s}_j) = \operatorname{cov}(\gamma_u(\mathbf{s}_i), \gamma_v(\mathbf{s}_j))$, $u, v = 1, 2$. The mean

structure $\boldsymbol{\mu}(\mathbf{s})$ can be modeled as $\boldsymbol{\mu}(\mathbf{s}) = \mathbf{X}(\mathbf{s})^T \boldsymbol{\beta}$, where

$$\mathbf{X}(\mathbf{s}) = \begin{bmatrix} \mathbf{X}_1(\mathbf{s})^T & \mathbf{0} \\ \mathbf{0} & \mathbf{X}_2(\mathbf{s})^T \end{bmatrix}$$

and $\boldsymbol{\beta} = \{\boldsymbol{\beta}_1, \boldsymbol{\beta}_2\}^T$ is a $(p_1 + p_2) \times 1$ vector of coefficients corresponding to the covariates.

Let $\mathbf{Z}_{vec} = \{Z_1(\mathbf{s}_1), \dots, Z_1(\mathbf{s}_N), Z_2(\mathbf{s}_1), \dots, Z_2(\mathbf{s}_N)\}^T$ be a $2N \times 1$ vector, \mathbf{C} is the cross-covariance matrix of order $2N \times 2N$, and

$$\mathbf{X} = \begin{bmatrix} \{\mathbf{X}_1(\mathbf{s}_1)^T, \dots, \mathbf{X}_1(\mathbf{s}_N)^T\}^T & \mathbf{0} \\ \mathbf{0} & \{\mathbf{X}_2(\mathbf{s}_1)^T, \dots, \mathbf{X}_2(\mathbf{s}_N)^T\}^T \end{bmatrix}$$

is a $2N \times (p_1 + p_2)$ matrix of covariates. Then with $\mathbf{V} = (\mathbf{X}^T \mathbf{C}^{-1} \mathbf{X})^{-1}$, the kriging prediction at an unobserved location \mathbf{s}_0 is

$$\hat{\mathbf{Y}}_{vec}(\mathbf{s}_0) = \mathbf{X}_0^T \hat{\boldsymbol{\beta}} + \mathbf{C}_0^T \mathbf{C}^{-1} (\mathbf{Z}_{vec} - \mathbf{X} \hat{\boldsymbol{\beta}})$$

where $\hat{\boldsymbol{\beta}} = \mathbf{V} \mathbf{X}^T \mathbf{C}^{-1} \mathbf{Z}_{vec}$, the generalized least square estimator of $\boldsymbol{\beta}$, $\mathbf{X}_0 = \mathbf{X}(\mathbf{s}_0)$ is the $2 \times (p_1 + p_2)$ matrix of covariates at location \mathbf{s}_0 , \mathbf{C}_0 is the $2N \times 1$ cross-covariance matrix between the response at location \mathbf{s}_0 and the observed locations.

The choice of cross-covariance functions in cokriging prediction plays a vital role in capturing the spatial dependence among locations and also among variables for multivariate data.

Among existing models, the multivariate Matérn cross-covariance function ([Apanaso-](#)

vich et al., 2012) is one of the most popular classes of Matérn covariance function. The parsimonious Matérn covariance function can be defined as

$$\mathbf{C}_{u,v}(\mathbf{h}) = \sigma_{uv}M\left(\mathbf{h}\left|\nu_{uv}, \sqrt{\alpha_{uv}^2}\right.\right), \quad \mathbf{h} = \mathbf{d}(\mathbf{s}_i, \mathbf{s}_j) \in \mathbb{R}, \quad (2)$$

where $\mathbf{d}(\mathbf{s}_i, \mathbf{s}_j) = \|\mathbf{s}_i - \mathbf{s}_j\|$ is the Euclidean distance between the locations, M is the Matérn correlation function (Cressie and Huang, 1999), ν is the smoothness, and α is the range parameter. Constraints on these parameters have been derived in Apanasovich et al. (2012).

Another example of a cross-covariance function is the linear model of coregionalization (LMC); (Genton and Kleiber, 2015). In this approach, a multivariate random field is represented as a linear combination of r independent random fields with potentially different spatial correlation functions. For $r = 2$, we can write the process $\boldsymbol{\gamma}(s)$ in terms of the latent processes as $\boldsymbol{\gamma}(\mathbf{s}) = \mathbf{A}\mathbf{U}(\mathbf{s})$, where \mathbf{A} is the 2×2 matrix of weights and $\mathbf{U}(\mathbf{s}) = \{U_1(\mathbf{s}), U_2(\mathbf{s})\}^T$, $\text{cov}(U_1, U_2) = 0$. Following this architecture, the LMC covariance function of a bivariate random field can be written as

$$\mathbf{C}_{ij}(\mathbf{h}) = \sum_{k=1}^r \rho_k(h) A_{ik} A_{jk}, \quad \mathbf{h} \in \mathbb{R}^d, \quad 1 \leq r \leq 2, \quad (3)$$

with $\rho_k(\cdot)$ as valid stationary correlation functions of $U_k(\cdot)$, and $A = (A_{ij})_{i,j=1}^{2,r}$ is a $2 \times r$ full-rank matrix.

Although cokriging is the best linear unbiased predictor, it suffers from several limitations. First, maximum likelihood estimation (MLE) for Gaussian processes requires

Cholesky factorization of the covariance matrix, which is computationally expensive, making it infeasible to implement traditional cokriging for large datasets. Moreover, many real-life datasets are non-Gaussian, and cokriging is not an optimal predictor in those scenarios.

2.2 DeepKriging for bivariate spatial data

DeepKriging, proposed by [Chen et al. \(2022\)](#), addresses these issues for univariate processes by rephrasing the problem as regression and introducing a spatially dependent neural network structure for spatial prediction. They have used the radial basis functions to embed the spatial locations into a vector of weights and passed them to the DNNs as inputs allowing them to capture the spatial dependence of the process. Similar to [Chen et al. \(2022\)](#), we propose to use spatial basis functions for the bivariate processes to construct the embedding layer instead of passing the coordinates of the observations directly to the NN. This idea is motivated by the multivariate Karhunen-Loève expansion ([Daw et al., 2022](#)) of a multivariate spatial random field, i.e., a bivariate spatial process $\boldsymbol{\gamma}(\mathbf{s})$ can be represented as

$$\boldsymbol{\gamma}(\mathbf{s}) = \sum_{b=1}^{\infty} \{w_{b,1}\phi_{b,1}(\mathbf{s}), w_{b,2}\phi_{b,2}(\mathbf{s})\}^T$$

where $w_{b,u}$'s are independent random variables and $\phi_{b,u}(\mathbf{s})$'s are the pairwise orthonormal basis functions corresponding to variable $u, u = 1, 2$. Therefore, a bivariate process can be approximated by

$$\boldsymbol{\gamma}(\mathbf{s}) \approx \sum_{b=1}^K \{w_{b,1}\phi_{b,1}(\mathbf{s}), w_{b,2}\phi_{b,2}(\mathbf{s})\}^T,$$

where the weights $w_{b,u}$ can be estimated by minimizing the risk function R . Hence the spatial problem can be viewed as multioutput linear regression (Borchani et al., 2015) with these basis functions $\phi_{b,u}$ as covariates.

Among many existing basis functions, such as spline basis functions (Wahba, 1990), wavelet basis functions (Vidakovic, 2009), and radial basis functions (Hastie et al., 2001), we have chosen the multi-resolution compactly supported Wendland radial basis function (Nychka et al., 2015) defined via $w(d) = \frac{(1-d)^6}{3}(35d^2 + 18d + 3)\mathbf{1}\{0 \leq d \leq 1\}$. The spatial basis functions are then defined as $\phi_i(\mathbf{s}) = w(\|\mathbf{s} - u_i\|/\theta)$ with θ as the bandwidth parameter and anchor points (spatial locations) $\{u_1, u_2, \dots, u_K\}$. We take $\{u_1, u_2, \dots, u_K\}$ to be a square grid of locations covering the spatial domain and θ to be 2.5 times the distance between adjacent anchor points. By selecting various K values, one can produce distinct sets of basis functions. This will enable us to record both the long- and short-range spatial dependencies. We must combine these basis functions into a single vector in order to send them to the neural network. See Chen et al. (2022) for detailed discussions on the basis function embedding. Therefore, these co-ordinates embedding can now be used as an input to the DNNs along with covariates $\mathbf{X}_{vec}(\mathbf{s}) = \{\mathbf{X}_1(\mathbf{s})^T, \mathbf{X}_2(\mathbf{s})^T\}^T$ which will better capture the spatial features of the data. Note that under our assumption of basis functions, $\phi_{.,1} = \phi_{.,2}$ for location \mathbf{s} , hence we can reduce our basis function set to $\phi(\mathbf{s}) = \{\phi_1(\mathbf{s}), \dots, \phi_K(\mathbf{s})\}^T$ where $\phi_b(\mathbf{s}) = \phi_{b,1}(\mathbf{s})$, $b = 1, 2, \dots, K$.

We have used a multi-output deep neural network structure to build the bivariate DeepKriging framework. We define $\mathbf{X}_\phi(\mathbf{s})$ as the vector of inputs containing the embedded vector of basis functions $\phi(\mathbf{s})$ and the covariates $\mathbf{X}_{vec}(\mathbf{s})$. Then $\mathbf{X}_\phi(\mathbf{s}) = (\phi(\mathbf{s})^T, \mathbf{X}_{vec}(\mathbf{s})^T)^T$.

Taking $\mathbf{X}_\phi(\mathbf{s})$ as the inputs to a neural network with L layers and M_l nodes in layer $l = 1, \dots, L$ DNN can be specified as,

$$\begin{aligned}
\mathbf{h}_1(\mathbf{X}_\phi(\mathbf{s})) &= \mathbf{W}_1 \mathbf{X}_\phi(\mathbf{s}) + \mathbf{b}_1, \quad \mathbf{a}_1(\mathbf{s}) = \psi(\mathbf{h}_1(\mathbf{X}_\phi(\mathbf{s}))) \\
\mathbf{h}_2(\mathbf{a}_1(\mathbf{s})) &= \mathbf{W}_2 \mathbf{a}_1(\mathbf{s}) + \mathbf{b}_2, \quad \mathbf{a}_2(\mathbf{s}) = \psi(\mathbf{h}_2(\mathbf{a}_1(\mathbf{s}))) \\
&\dots \\
\mathbf{h}_L(\mathbf{a}_{L-1}(\mathbf{s})) &= \mathbf{W}_L \mathbf{a}_{L-1}(\mathbf{s}) + \mathbf{b}_L, \quad \mathbf{f}_{NN}(\mathbf{X}_\phi(\mathbf{s})) = \mathbf{h}_L(\mathbf{a}_{L-1}(\mathbf{s})),
\end{aligned} \tag{4}$$

where $\mathbf{f}_{NN}(\mathbf{X}_\phi(\mathbf{s})) = \{f_{NN_1}(\mathbf{X}_\phi(\mathbf{s})), f_{NN_2}(\mathbf{X}_\phi(\mathbf{s}))\}^T$ is the prediction output from the model, the weight matrix \mathbf{W}_l is a $M_l \times M_{l-1}$ matrix of parameters and \mathbf{b}_l , a $M_l \times 1$ vector is the bias at layer l . The parameter set of this network is $\boldsymbol{\theta} = \{\mathbf{W}_l, \mathbf{b}_l : l = 1, 2, \dots, L\}$. $\psi(\cdot)$ signifies the activation function which in our case is the rectified linear unit ReLU (Schmidt-Hieber, 2020). The final layer does not contain any activation function and provides just the linear output allowing it to take any value in \mathbb{R}^2 .

Figure 1 gives a graphical illustration of the spatially dependent neural network structure.

The Bivariate DeepKriging (**Biv.DeepKriging**) is a multivariate extension of the univariate DeepKriging. Here we propose to approximate the optimal predictor $\hat{Y}^{opt}(\mathbf{s}_0)$ with the help of deep neural network structure, i.e; $\hat{Y}^{opt}(\mathbf{s}_0) \approx \mathbf{f}_{NN}(\mathbf{X}_\phi(\mathbf{s}_0))$ We define the optimal neural network based predictor as $\mathbf{f}_{NN}^{opt}(\mathbf{X}_\phi(\mathbf{s}_0)) = \operatorname{argmin}_{\mathbf{f}_{NN}} R(\mathbf{f}_{NN}(\mathbf{X}_\phi(\mathbf{s}_0)) | \mathbf{Z}_N)$. where $\mathbf{f}_{NN} \in \mathcal{F}$ is a multioutput function in the domain of functions \mathcal{F} which are feasible by the defined neural network structure. Note that here \mathbf{f}_{NN} is conditioned on the param-

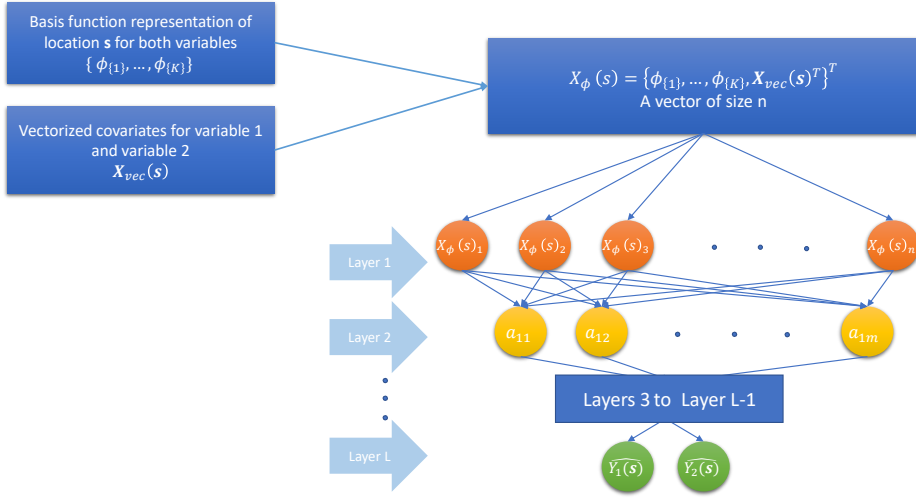


Figure 1: Structure of the spatially dependent neural network with embedding

eter θ . Hence, one can estimate $\mathbf{f}_{NN}^{opt}(\cdot)$ by minimizing the empirical version of the risk function $R(\cdot)$ based on θ given as

$$R\{\mathbf{f}_{NN}(\mathbf{X}_\phi(\mathbf{s}))|\theta, \mathbf{Z}_N\} = \frac{1}{N} \sum_{n=1}^N M(\mathbf{s}_n), \quad (5)$$

where $M(\mathbf{s}_n) = \frac{w_1 \times (f_{NN1}(\mathbf{X}_\phi(\mathbf{s})) - Z_1(\mathbf{s}_n))^2 + w_2 \times (f_{NN2}(\mathbf{X}_\phi(\mathbf{s})) - Z_2(\mathbf{s}_n))^2}{2}$. and $w_u \propto \sigma_u^2$, $u = 1, 2$.

We have chosen $w_u = \frac{1}{\sigma_u^2}$. Here σ_u^2 is unknown and can be estimated through the sample variance of the u -th variable. The final predictor of the neural network would be the bivariate prediction vector $\mathbf{f}_{NN}^{opt}(\mathbf{X}_\phi(\mathbf{s}_0))$ where

$$\hat{\theta} = \underset{\theta}{\operatorname{argmin}} R\{\mathbf{f}_{NN}(\mathbf{X}_\phi(\mathbf{s}))|\theta, \mathbf{Z}_N\}.$$

2.3 The link between Bivariate DeepKriging and LMC

For the univariate case, [Chen et al. \(2022\)](#) established a connection between DeepKriging and Kriging. They demonstrated that fixed rank kriging (FRK) ([Cressie and Johannesson, 2008](#)) is a linear function of covariates and basis functions, representing a special case of DeepKriging with one layer when all activation functions are set to be linear.

Theorem: For a co-located bivariate spatial process, assuming that the latent variables are constructed with the same sets of basis functions, the Linear Model of Co-regionalization (LMC) represents a special case of **Biv.DeepKriging**.

Proof: For the bivariate case, the construction of LMC ([Genton and Kleiber, 2015](#)) provides insights into such a link. The underlying bivariate spatial process $\boldsymbol{\gamma}(\mathbf{s})$ can be written as

$$\boldsymbol{\gamma}(\mathbf{s}) = \mathbf{A}\mathbf{U}(\mathbf{s}),$$

where $\mathbf{A} = \begin{bmatrix} a_{11} & a_{12} \\ a_{21} & a_{22} \end{bmatrix}$ and $\mathbf{U}(\mathbf{s}) = \{U_1(\mathbf{s}), U_2(\mathbf{s})\}$ with $cov(U_1(\mathbf{s}), U_2(\mathbf{s})) = 0$.

Now, using the Karhunen-Loève Theorem ([Adler, 2010](#)), we can approximate them as

$$U_1(\mathbf{s}) = \sum_{b=1}^K w_{1,b} \phi_{1,b}(\mathbf{s})$$

and

$$U_2(\mathbf{s}) = \sum_{b=1}^K w_{2,b} \phi_{2,b}(\mathbf{s}).$$

We then write

$$\begin{aligned}
\boldsymbol{\gamma}(\mathbf{s}) &= \mathbf{A}\mathbf{U}(\mathbf{s}) \\
&= \begin{bmatrix} a_{11} & a_{12} \\ a_{21} & a_{22} \end{bmatrix} \begin{bmatrix} U_1(\mathbf{s}) \\ U_2(\mathbf{s}) \end{bmatrix} \\
&= \begin{bmatrix} a_{11} \sum_{b=1}^K w_{1,b} \phi_{1,b}(\mathbf{s}) + a_{12} \sum_{b=1}^K w_{2,b} \phi_{2,b}(\mathbf{s}) \\ a_{21} \sum_{b=1}^K w_{1,b} \phi_{1,b}(\mathbf{s}) + a_{22} \sum_{b=1}^K w_{2,b} \phi_{2,b}(\mathbf{s}) \end{bmatrix} \\
&= \begin{bmatrix} \sum_{b=1}^K (a_{11} w_{1,b} \phi_{1,b}(\mathbf{s}) + a_{12} w_{2,b} \phi_{2,b}(\mathbf{s})) \\ \sum_{b=1}^K (a_{21} w_{1,b} \phi_{1,b}(\mathbf{s}) + a_{22} w_{2,b} \phi_{2,b}(\mathbf{s})) \end{bmatrix}.
\end{aligned}$$

Now, as both the random variables $U_1(\mathbf{s})$ and $U_2(\mathbf{s})$ are co-located, we can choose the same set of basis functions for them, resulting in

$$\begin{aligned}
&= \begin{bmatrix} \sum_{b=1}^K (a_{11} w_{1,b} + a_{12} w_{2,b}) \phi_b(\mathbf{s}) \\ \sum_{b=1}^K (a_{21} w_{1,b} + a_{22} w_{2,b}) \phi_b(\mathbf{s}) \end{bmatrix}, \text{ writing } \phi_{1,b}(\mathbf{s}) = \phi_{2,b}(\mathbf{s}) = \phi_b(\mathbf{s}) \\
&= \mathbf{W}_1 \boldsymbol{\phi}(\mathbf{s}).
\end{aligned}$$

which is a multioutput regression with $\boldsymbol{\phi}(\mathbf{s})$ as covariates and $\boldsymbol{\gamma}(\mathbf{s})$ as the response, which is same as (4) with $L = 1$, $\mathbf{b}_1 = \mathbf{0}$, and a linear activation function.

2.4 Prediction uncertainty

The utilization of neural networks for uncertainty quantification has garnered significant attention in recent years. Various prominent techniques have emerged (Khosravi et al., 2011;

Nourani et al., 2021) to enhance the estimation of prediction intervals. For instance, Cannon and Whitfield (2002) and Jeong and Kim (2005) employed ensemble DNNs for forming prediction intervals, while Srivastav et al. (2007) and Boucher et al. (2009) introduced bootstrap-based uncertainty quantification for DNNs. Additionally, Kasiviswanathan and Sudheer (2016) proposed a Bayesian framework for uncertainty quantification with DNNs.

The univariate DeepKriging model computed prediction intervals using a histogram-based approximation to the predictive distribution. Nonetheless, this method exhibits several limitations. Firstly, the accuracy of the prediction intervals heavily relies on the choice of bins for the histogram. The selection of cut points in the histogram, which are randomly chosen from a uniform distribution, may impact the approach’s performance. Moreover, the computational time increases when training a large number of ensemble models, and the ensemble approach suggested by this model might fail to capture the variation in the data. In this section, we propose an uncertainty quantification method to address these limitations.

For the bivariate spatial prediction problem, utilizing (1) and (4), the prediction at an unobserved location \mathbf{s}_0 can be expressed as

$$\hat{\mathbf{Z}}(\mathbf{s}_0) = \mathbf{f}_{NN}^{opt}(\mathbf{X}_\phi(\mathbf{s}_0)) + \boldsymbol{\epsilon}(\mathbf{s}_0).$$

By employing ensembles, we can generate B replications of $\hat{\mathbf{Z}}(\mathbf{s}_0)$ at \mathbf{s}_0 . Consequently,

the prediction can be articulated as

$$\begin{aligned}\hat{\mathbf{Z}}(\mathbf{s}_0)^B &= \left(\frac{1}{B} \sum_{i=1}^B \hat{Z}_1(\mathbf{s}_0)_i, \frac{1}{B} \sum_{i=1}^B \hat{Z}_2(\mathbf{s}_0)_i \right)^T \\ &= \left(\frac{1}{B} \sum_{i=1}^B (f_{NN_1}^{opt}(\mathbf{X}_\phi(\mathbf{s}_0)) + \epsilon_1(\mathbf{s}_0))_i, \frac{1}{B} \sum_{i=1}^B (f_{NN_2}^{opt}(\mathbf{X}_\phi(\mathbf{s}_0)) + \epsilon_2(\mathbf{s}_0))_i \right)^T.\end{aligned}\quad (6)$$

Employing the multidimensional Central Limit Theorem yields $\hat{\mathbf{Z}}(\mathbf{s}_0)^B \sim \mathcal{N}_2(\mathbf{Z}(\mathbf{s}_0), \frac{1}{B}\Sigma_{\mathbf{Z}(\mathbf{s}_0)})$.

The variance term associated with $Z_u(\mathbf{s}_0)$, for $u = 1, 2$, is $\sigma^2(Z_u(\mathbf{s}_0)) = \text{Var}(Y_u(\mathbf{s}_0)) + \text{Var}(\epsilon_u(\mathbf{s}_0))$, assuming independence between $Y_u(\mathbf{s}_0)$ and $\epsilon_u(\mathbf{s}_0)$. From the outcomes of B ensembles, we can express $\widehat{\text{Var}}(Y_u(\mathbf{s}_0))$ as

$$\widehat{\text{Var}}(Y_u(\mathbf{s}_0)) = \frac{1}{B-1} \sum_{i=1}^B f_{NN_u}^{opt}(\mathbf{X}_\phi(\mathbf{s}_0))_i^2 - \left(\frac{1}{B} \sum_{i=1}^B f_{NN_u}^{opt}(\mathbf{X}_\phi(\mathbf{s}_0))_i \right)^2. \quad (7)$$

The noise variance $\text{Var}(\epsilon_u(\mathbf{s}_0))$ can be represented as

$$\begin{aligned}\text{Var}(\epsilon_u(\mathbf{s}_0)) &= \text{Total Variance} - \text{Model variance} \\ &= \mathbb{E}\{(Z_u(\mathbf{s}_0) - \hat{Z}_u(\mathbf{s}_0))^2\} - \widehat{\text{Var}}(Y_u(\mathbf{s}_0)).\end{aligned}$$

An empirical approximation of the above is

$$r_u^2(\mathbf{s}_0) = \max\left\{ \left(Z_u(\mathbf{s}_0) - \frac{1}{B} \sum_{i=1}^B f_{NN_u}^{opt}(\mathbf{X}_\phi(\mathbf{s}_0))_i \right)^2 - \widehat{\text{Var}}(Y_u(\mathbf{s}_0)), 0 \right\}, \quad u = 1, 2. \quad (8)$$

Consequently, based on the above formulation, the prediction interval at the α level of

significance for variable u at location \mathbf{s}_0 can be given as,

$$\hat{Z}_u(\mathbf{s}_0)^B \pm t_{(1-\alpha/2),df} \sqrt{\frac{1}{B} \left(\widehat{\text{Var}}(Y_u(\mathbf{s}_0)) + r_u^2(\mathbf{s}_0) \right)}, \quad u = 1, 2 \quad (9)$$

where $t_{(1-\alpha/2),df}$ represents the $1 - \alpha/2$ quantile of the t -distribution with df degrees of freedom, $df = N - p$, where p denotes the number of estimated parameters.

In connection with the preceding explanation, we now provide a comprehensive definition of the algorithm for calculating the prediction interval. We partition our training dataset D into two subsets, D_1 and D_2 . From D_1 , we extract a sample D_{11} . Initially, we train a neural network model with L layers using the dataset D_{11} , and then proceed to draw B bootstrap samples from D_1 to train B DNN models. For these B bootstrap fits, we keep the weights fixed for the first L_0 layers, allowing only the new models to be trained based on the last $L - L_0$ layers. This approach is adopted to control the degrees of freedom of the t -distribution in (9). By exclusively re-training the last $L - L_0$ layers, we ensure that the total number of trainable parameters p in each bootstrap computation remains smaller than N . Following this procedure, we compute $\hat{Z}_u(\mathbf{s}_0)$ and $\widehat{\text{Var}}(Y_u(\mathbf{s}_0))$ based on the training data D_1 . Since we know $\mathbb{E}\epsilon_u(\mathbf{s}_0) = 0$, we have $\hat{Z}_u(\mathbf{s}_0) = \frac{1}{B} \sum_{i=1}^B fNN_u^{opt}(\mathbf{X}_\phi(\mathbf{s}_0))$.

Computation of $r_u^2(\mathbf{s}_0)$ as defined in (8) is infeasible as we do not have $Z_u(\mathbf{s}_0)$. Hence we estimate $r_u^2(\mathbf{s}_0)$ through the second part of the training dataset D_2 . To do this we use the nearest neighbour approach. We obtain a set $D_{20} = \{\mathbf{s}_k : \mathbf{s}_k \in D_2\}$ with cardinality G

of locations closest to \mathbf{s}_0 and take average of the corresponding $r_u^2(\mathbf{s}_k)$'s, i.e.,

$$\hat{r}_u^2(\mathbf{s}_0) = \frac{1}{G} \sum_{\mathbf{s}_g \in D_{20}} r_u^2(\mathbf{s}_g), \quad (10)$$

such that \mathbf{s}_g 's are the nearest G locations to \mathbf{s}_0 .

Algorithm 1 provides a step-by-step explanation of our prediction interval construction method.

Algorithm 1 Prediction Intervals Algorithm

Split \mathbf{D} into \mathbf{D}_1 and \mathbf{D}_2 equally.

Further split \mathbf{D}_1 into \mathbf{D}_{11} and \mathbf{D}_{12} .

Train a deep neural network (**DNN**) of L layers on \mathbf{D}_{11} .

Take \mathbf{B} random samples $\{\mathbf{D}_1^1, \mathbf{D}_1^2, \dots, \mathbf{D}_1^{\mathbf{B}}\}$ from \mathbf{D}_1 .

for $i \leftarrow 1$ to \mathbf{B} **do**

Fix the weights of the first L_0 layers of the **DNN** and train the last $L - L_0$ layers on \mathbf{D}_1^i .

Train the **DNN** on \mathbf{D}_1^i and store the result. Denote it as $\mathbf{f}_{NN}^{opt}(\mathbf{X}_\phi(\mathbf{s}))_i$.

end for

for location \mathbf{s}_k in \mathbf{D}_2 **do**

Calculate $\hat{Z}_u(\mathbf{s}_k)^B$ (6) and $Var(\widehat{Y}_u(\mathbf{s}_k))$ (7).

Calculate $r_u^2(\mathbf{s}_k)$ (8).

end for

For test location \mathbf{s}_0 , obtain the set $\mathbf{D}_{20} = \{\mathbf{s}_k : \mathbf{s}_k \in \mathbf{D}_2\}$ of the nearest G locations from \mathbf{s}_0 .

Calculate $\hat{Z}_u(\mathbf{s}_0)^B$ (6), $Var(\widehat{Y}_u(\mathbf{s}_k))$ (7), and $\hat{r}_u^2(\mathbf{s}_0)$ (10).

Calculate the prediction interval as defined in (9).

▷ Where u stands for the u -th variable, $u = 1, 2$.

2.5 Computational scalability

To better understand the computational benefits of DNN over traditional kriging we can look at the time complexity of the DNN with kriging. DeepKriging involves matrix multiplication in several layers to give us the resulting output. Whereas, kriging involves a

$2N \times 2N$ matrix inversion. Note that, time complexity of multiplication of one $m \times n$ and $n \times p$ matrix is $O(mnp)$. So a single layer l of the neural network with minibatch (a minibatch (Hinton et al., 2012) is a randomly selected portion of the data used for neural network training.) size of b , M_{l-1} input nodes and M_l output nodes will have the time complexity of $O(bM_{l-1}M_l)$. Faster training is made possible by defining a minibatch. Hence a neural network with L layers will have time complexity $O(\sum_{l=1}^L bM_{l-1}M_l)$. On the other hand, time complexity of Kriging is $O(8N^3)$. Hence for large N deep kriging with adequate number of layers and nodes is more computationally efficient than traditional kriging.

3 Simulation studies

3.1 Point predictions

We have conducted several experiments through Gaussian, non-Gaussian and nonstationary simulations to give a comprehensive comparison of our proposed method with the parsimonious bivariate Matérn (**CoKriging.Matérn**) as well as the linear model of coregionalization (**CoKriging.LMC**). In order to compare our results we have computed the Root Mean Square Prediction Error for each variable as the validation metric. For N locations this can be given as

$$\mathbf{MSPE}_u = \frac{1}{N} \sum_{n=1}^N (Z_u(\mathbf{s}_n) - \hat{Z}_u(\mathbf{s}_n))^2, \quad u = 1, 2.$$

Our model performed at par with **CoKriging.Matérn** and **CoKriging.LMC** in the Gaussian scenario. Details of the study has been provided in the supplementary materials.

In this section we mainly concentrate on non-Gaussian and nonstationary scenarios where **Biv.DeepKriging** clearly outperforms the traditional statistical techniques.

Here we consider two simulation settings. The first one is bivariate non-Gaussian with covariates. We simulated the model from the following framework

$$\mathbf{Y}(\mathbf{s}) = \boldsymbol{\mu}(\mathbf{s}) + \boldsymbol{\gamma}(\mathbf{s}),$$

where $\boldsymbol{\mu}(\mathbf{s})$ is the mean function and $\boldsymbol{\gamma}(\mathbf{s})$ follows a non-Gaussian distribution. We define $\boldsymbol{\mu}(\mathbf{s}) = \{\mu_1(\mathbf{s}), \mu_2(\mathbf{s})\}$ as a complex function of covariates given as:

$$\begin{aligned} \mu_u(\mathbf{s}) = & x_1(\mathbf{s})^2 - x_2(\mathbf{s})^2 + x_3(\mathbf{s})^2 - x_4(\mathbf{s})^2 - \\ & x_5(\mathbf{s})^2 + 2x_1(\mathbf{s})x_2(\mathbf{s}) + 3x_2(\mathbf{s})x_3(\mathbf{s}) - 2x_3(\mathbf{s})x_5(\mathbf{s}) + \\ & 10x_1(\mathbf{s})x_4(\mathbf{s}) + \sin(x_1(\mathbf{s}))x_2(\mathbf{s})x_3(\mathbf{s}) + \\ & \cos(x_2(\mathbf{s}))x_3(\mathbf{s})x_5(\mathbf{s}) + (x_1(\mathbf{s})x_2(\mathbf{s})x_4(\mathbf{s})x_5(\mathbf{s})), u = 1, 2 \end{aligned}$$

where the covariates $x_i(\mathbf{s}), i = 1, \dots, 5$ were generated from multivariate Gaussian distributions with Matérn covariance with varying parameters. $\boldsymbol{\gamma}(\mathbf{s})$ was simulated from a multivariate Gaussian distribution with parsimonious Matérn covariance (2) with parameters $\sigma_1 = 0.7, \sigma_2 = 0.8, \nu_1 = 0.3, \nu_2 = 0.6, \alpha_1^2 = 0.05, \alpha_2^2 = 0.1, R = 0.5$. We generated 100 replicates of the random field at 1200 irregular locations on $[0, 1] \times [0, 1]$ by transforming the Gaussian fields from the previous simulation using the Tukey-g and h transformation

(Xu and Genton, 2017) defined as

$$\tau_{g,h}(z) = g^{-1}\{\exp(gz) - 1\}\exp(hz^2/2),$$

with $g = 0.8, h = 0.5$ for variable 1 and $g = -0.8, h = 0.5$ for variable 2.

Figure 2 illustrates the boxplot of **MSPE** for the two variables across 100 replicates. The superiority of **Biv.DeepKriging** over other conventional approaches is evident from the boxplots. It's worth noting that due to parameter configurations and data sample paths, optimization in **CoKriging.Matérn** and **CoKriging.LMC** may present challenges. In contrast, **Biv.DeepKriging** is devoid of such limitations and can be readily implemented on any dataset.

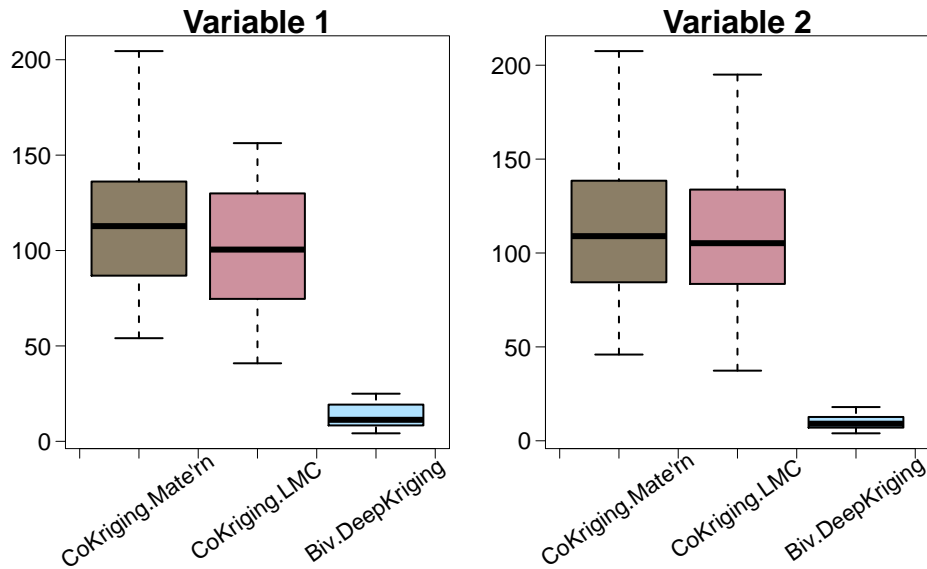


Figure 2: Boxplot of **MSPE** for the three different models **CoKriging.Matérn**, **CoKriging.LMC** and **Biv.DeepKriging** over 100 replicates for the non-Gaussian simulation.

The second simulation explores nonstationary datasets. We simulate nonstationary random fields using the Wendland radial basis functions as discussed in Section 2.2. We

apply a nonlinear transformation to the basis functions to obtain the nonstationary fields, defined as

$$Y_1(\mathbf{s}) = \sum_{i=1}^{19} \left((a \cdot \phi_{2i}(\mathbf{s})^{3/2} + c \cdot \phi_{2i-1}(\mathbf{s})) - b \cdot \sqrt{\phi_{2i}(\mathbf{s}) \cdot \phi_{2i-1}(\mathbf{s})} \right)$$

$$Y_2(\mathbf{s}) = \sum_{i=1}^{19} \left((d \cdot \phi_{2i}(\mathbf{s}) - e \cdot \phi_{2i-1}(\mathbf{s})^{3/2}) \right)$$

where parameters $\{a, b, c, d, e\} \sim \text{Uniform}(-2.5, 2.5)$.

Figure 3 displays the RMSPE over 100 replicates. It is evident that **Biv.DeepKriging** significantly outperforms the other comparative methods.

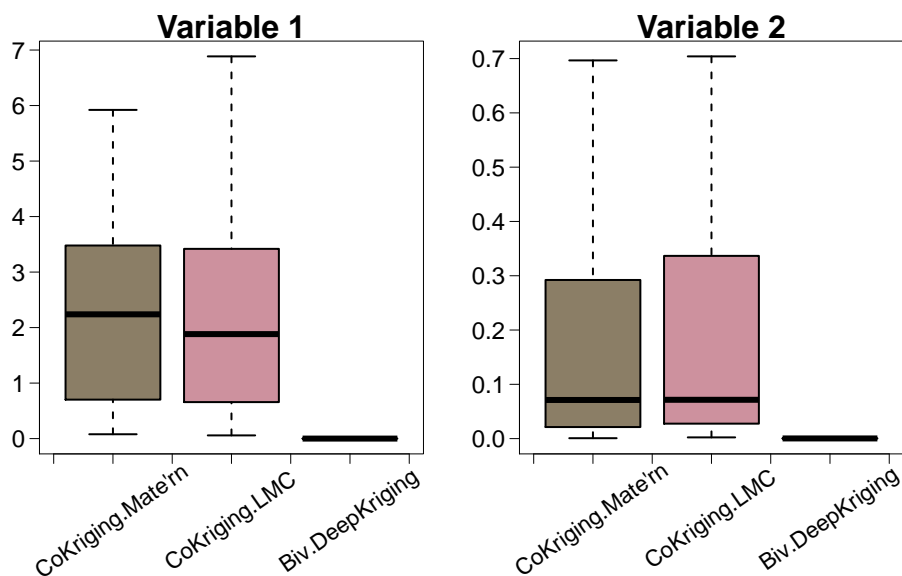


Figure 3: Boxplot of MSPE for the three different models **CoKriging.Matérn**, **CoKriging.LMC** and **Biv.DeepKriging** over 100 replicates for the nonstationary simulation.

3.2 Prediction intervals

Several studies (Ho et al., 2001; Zhao et al., 2008) have proposed various approaches for quantifying the quality of the prediction interval. We have chosen here two specific measures

for comparison of the prediction bands, namely prediction interval coverage probability (PICP) and mean prediction interval width (MPIW). In mathematical notations

$$PICP_u = \frac{1}{N} \sum_{j=1}^N \mathbf{1}_{Z_u(s_j) \in [L_u(s_j), U_u(s_j)]}, \quad MPIW_u = \frac{1}{N} \sum_{j=1}^N [U_u(s_j) - L_u(s_j)], \quad u = 1, 2 \quad (11)$$

where $(L_u(s), U_u(s))$ are the lower and upper prediction bounds for variable u at location s and n is the number test samples.

In this section we evaluate our proposed approach of the prediction interval computation with the parametric prediction intervals obtained from cokriging models. We have computed the prediction interval validation metrics (11) for the comparative models using the same set of simulations as defined in 3.1. In all of the following assessments we have computed the 95% prediction bound for predictions in the test set.

Table 1 shows the results for all the simulation scenarios. It can be seen that for the Gaussian simulations where **CoKriging.Matérn_{true}** is optimal the **Biv.DeepKriging** model gives comparable performance. For non-Gaussian and non-stationary scenarios clearly the **Biv.DeepKriging** outperforms the other methods by attaining the 95% prediction with smaller width. Note that, some of the simulation scenarios

Table 1: Comparison on both the variables over different simulation settings.

Simulation type	Models	MSPE ₁	SE ₁	PICP ₁	MPIW ₁	MSPE ₂	SE ₂	PICP ₂	MPIW ₂
Gaussian	CoKriging.Matérn_{true}	0.23	0.11	0.95	0.87	0.21	0.09	0.95	0.92
	Biv.DeepKriging	0.24	0.19	0.94	0.98	0.24	0.18	0.95	1.07
non-Gaussian	CoKriging.Matérn	12.1 ($\times 10$)	0.29 ($\times 10$)	0.27	6.21	12.4 ($\times 10$)	0.49 ($\times 10$)	0.26	6.16
	CoKriging.LMC	87.4	12.13	0.58	11.2	94.5	21.9	0.51	9.99
	Biv.DeepKriging	32.7	11.6	0.94	29.9	23.8	9.11	0.94	29.4
non-stationary	CoKriging.Matérn	1.95	0.75	0.92	3.53	0.13	0.02	0.09	1.01
	CoKriging.LMC	1.26	0.14	0.92	3.49	0.14	0.02	0.10	1.33
	Biv.DeepKriging	7.52 ($\times 10^{-4}$)	1.01 ($\times 10^{-4}$)	0.96	0.16	6.83 ($\times 10^{-4}$)	1.08 ($\times 10^{-4}$)	0.95	0.19

While Section 3.1 demonstrates how the nonlinearity in **Biv.DeepKriging** aids in cap-

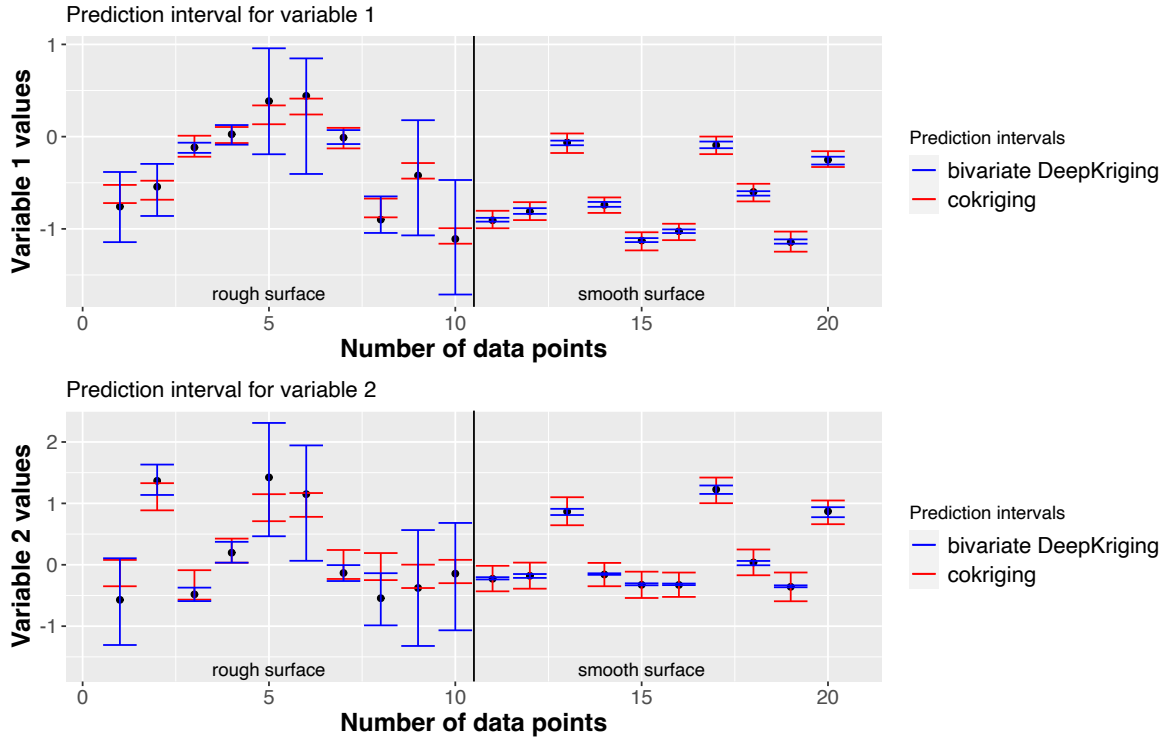


Figure 4: Prediction interval for variable 1 and variable 2 for the nonstationary simulation. Here the red interval signifies the prediction interval generated by **CoKriging.Matérn** and the blue interval is for **Biv.DeepKriging**.

turing the nonstationarity in the data, it's equally important to showcase the improvement in prediction intervals offered by the proposed **Biv.DeepKriging** model. To investigate this, we generate nonstationary data with a nonstationary mean function. The simulation details are provided in supplementary materials. The dataset depicted in Figure 10 exhibits a rough surface in the lower left and a smooth surface in the upper right.

Figure 4 displays the prediction intervals for **Biv.DeepKriging** and the cokriging models for the nonstationary simulation. The prediction intervals for **Biv.DeepKriging** adapt spatially. Specifically, **Biv.DeepKriging** offers wider prediction bounds for regions with higher variance, whereas it provides narrower prediction bounds for regions with lower variability.

3.3 Computation time

Based on the same simulation setting we investigate the computational time of **Biv.DeepKriging** compared to **CoKriging.Matérn** with different number of observations N . We have fully optimized the model and have measured the computation time for the whole process in each case. We have also compared **CoKriging.Matérn** with both of our proposed methods for point prediction as well as interval prediction. Figure 5 shows the comparison

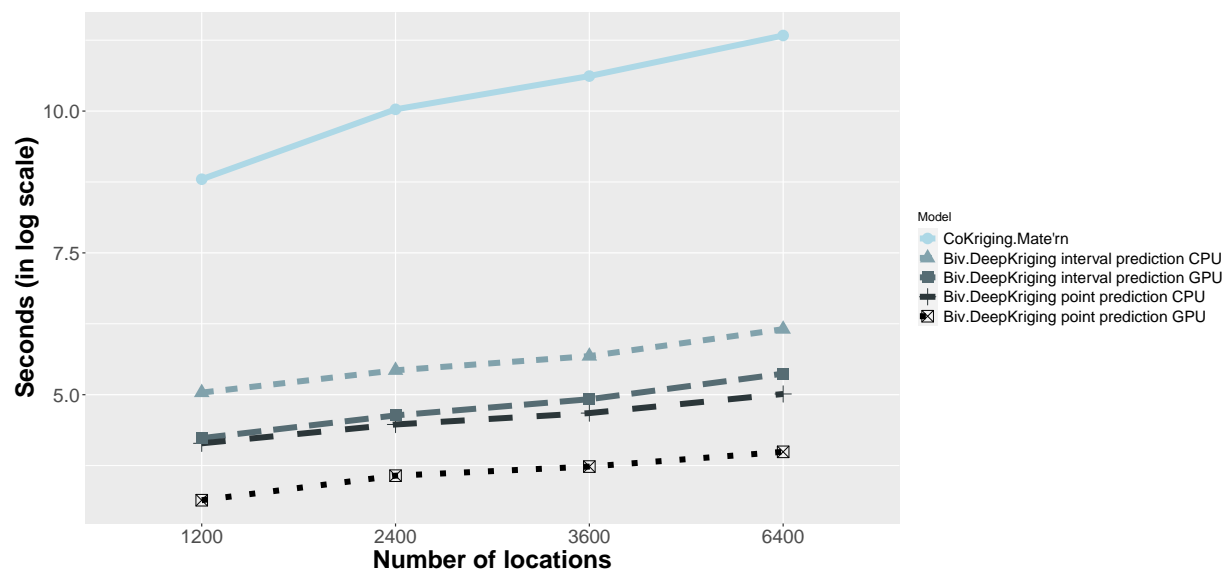


Figure 5: Total computation time (in seconds) for different models in log scale for different number of locations

results. As it can be seen **Biv.DeepKriging** always outperforms **CoKriging.Matérn** in computational time hence it is much more scalable when the sample size increases. For example, when $N = 6400$, which is the largest sample size we have considered, it takes more than 23 hours (83,484 seconds) to train the cokriging model, which makes it computational infeasible for larger N . However, for the same data size, **Biv.DeepKriging** with prediction interval only costs 7.85 minutes (471 seconds) without GPU acceleration and 3.58 minutes

(215 seconds) with a Tesla P100 GPU. We used the GPU from Ibex a shared computing platform at KAUST. For a more powerful GPU, the computational cost will be further reduced.

4 Application

In recent years, Saudi Arabia is seeking to reduce its reliance on fossil fuels for energy demand by investing in renewable energy sources. To achieve this goal, they have introduced several milestones for their upcoming smart cities. For King Abdullah City for Atomic and Renewable Energy (KA-CARE, 2012) they are planning for 54 GW of renewable energy portfolio by 2032, of which 9 GW will come from wind power. The Saudi Vision 2030 (2016) aims at achieving 9.5 GW of renewable energy by 2023. NEOM, an acronym for "New Future" and "New Enterprise Operating Model", is the upcoming mega-city project for Saudi Arabia which is planned to use only renewable power sources (wind and solar). For instance, wind turbines are widely used throughout the world to produce wind energy. However, installing such turbines necessitates precise measurements of the local wind direction and speed. To achieve this goal, an accurate wind speed interpolation model is crucial.

The majority of previous publications modeled wind data using geostatistical methods. Kriging was employed by [Wang et al. \(2020\)](#) to model wind fields. Large wind datasets were modeled for interpolation by [Salvaña et al. \(2021\)](#) using the ExaGeoStat software, which uses bivariate parsimonious Matérn covariance structure. However, these techniques always presumptively assume that the data are stationary and Gaussian. In this paper we

propose a novel methodology to model the bivariate wind speed which can then be used for spatial prediction and get high resolution maps of wind fields in any particular region. For our application we have also provided a high resolution wind interpolation for the NEOM region.

We have fitted **Biv.DeepKriging** on the wind data discussed in Supplementary materials. We have used 3 layers of basis functions with $K = 100, 361, 1369$ respectively. The neural network consists of $L = 7$ layers with $M_1 = M_2 = M_3 = M_4 = 100$ for first 4 layers, $M_5 = 50, M_6 = 50$ and $M_7 = 2$ nodes in the final layer. By using a sample from a uniform distribution, the model weights were initialized, and a learning rate of 0.01 was selected. The dataset consists of 506,771 locations. However, due to computational issues, the cokriging models could only handle a small subsample of the data. For this reason, we have randomly chosen 147,000 locations for training of the cokriging model. On the other hand, the **Biv.DeepKriging** can easily handle the full data. Hence we have fitted two different sets of models with deep neural networks, first with 147,000 (**Biv.DeepKriging**₁₄₇₀₀₀) and second with 450,000 (**Biv.DeepKriging**₄₅₀₀₀₀) locations and we randomly chosen 1000 locations from the rest for testing. To make the cokriging model more competitive and to reduce the computational burden, we have splitted the data into 100 sub-regions and fitted the model on each sub-region independently.

Table 2 shows that **Biv.DeepKriging** outperforms **CoKriging.Matérn** in MSPE.

Table 2: MSPE for **CoKriging.Matérn** and **Biv.DeepKriging**.

Models	RMSPE ₁	RMSPE ₂
CoKriging.Matérn	0.882	4.066
Biv.DeepKriging ₁₄₇₀₀₀	0.488	0.438
Biv.DeepKriging ₄₅₀₀₀₀	0.394	0.392

Next we look at the 95% prediction intervals provided by **Biv.DeepKriging** and **CoKriging.Matérn**. From Table 3 we can see that even though the MPIW for **CoKriging I** is smaller than **Biv.DeepKriging**, it fails drastically containing the true values within its bounds.

Table 3: PICP and MPIW with **CoKriging.Matérn** and **Biv.DeepKriging** for variable 1 and variable 2 respectively.

Models	$PICP_1$	$PICP_2$	$MPIW_1$	$MPIW_2$
CoKriging.Matérn	0.601	0.734	1.671	1.343
Biv.DeepKriging	0.971	0.950	1.226	1.340

We have also captured the total computation time using **Biv.DeepKriging** and **CoKriging I**. For **CoKriging I** total computation time was 2.18 days (188,352 seconds) where as for **Biv.DeepKriging** it took **16.81 minutes** (1009 seconds) for point prediction and **55.61 minutes** (3337 seconds) for interval prediction.

4.1 Spatial interpolation of wind field data

We have given a high resolution interpolation (from $5km \times 5km$ to $1km \times 1km$) for the region near NEOM, an upcoming smart city in Saudi Arabia. This downscaling can improve our understanding of the wind patterns. [Sanchez Gomez and Lundquist \(2020\)](#) have explored how the change in wind direction affect wind turbine performance. Hence understanding the exact wind patterns in a high resolution field will help in wind energy setup in the area. Figure 6 gives a visual representation of the spatial interpolation carried out using **Biv.DeepKriging**.

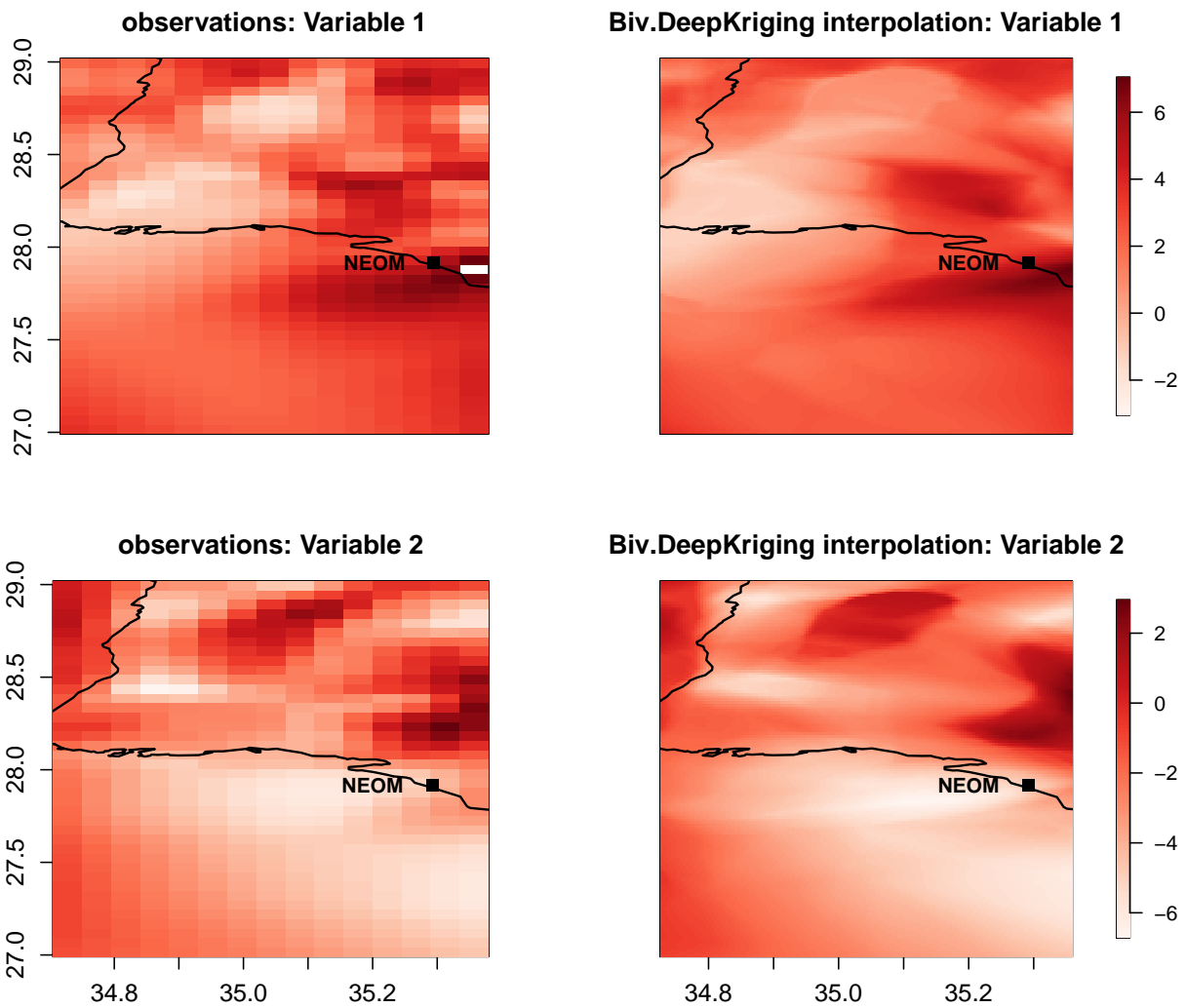


Figure 6: Spatial downscaling from resolution of $5km \times 5km$ to $1km \times 1km$ of the U and V component of wind over the region NEOM

5 Discussion

In this work, we have extended the univariate DeepKriging to bivariate scenario for spatial prediction without any parametric assumption of the underlying distribution of the data. We have also introduced a nonparametric approach for prediction interval computation for this deep learning based spatial modelling architecture. Our model is generally compatible with non-stationarity, non-linear relationships, and non-Gaussian data.

In our implementation we have chosen radial basis functions for spatial embedding. However for long range spatial dependence and circular covariance structures choice of other basis functions such as smoothing spline basis functions (Wahba, 1990), wavelet basis functions (Vidakovic, 2009) can be explored.

The loss function used to **Biv.DeepKriging** is a weighted MSE where weights are proportional to the variance of the variables. More complex weights can be incorporated to capture complex terrain behaviours. In our study we have not considered topographical elevation. This can be incorporated by using relevant covariates or by creating an adaptive loss function.

An interesting avenue of future work for prediction intervals is to extend the conformal prediction methods of Mao et al. (2020) to the deepKriging case. This method is model free and thus would avoid the assumption that the prediction intervals are a symmetric t-distribution.

In environmental modeling, interpretability plays a crucial role. When employing deep neural network architectures, one straightforward approach to interpretability involves examining the weight matrix of the input layer. This matrix often provides a basic under-

standing of the significance of specific covariates. For instance, if the weights corresponding to certain covariates are close to zero, it suggests that their influence on the model output is minimal. Recent developments in interpretability include techniques such as Shapley values (Merrick and Taly, 2020) and Local Interpretable Model-Agnostic Explanations (LIME) (Zafar and Khan, 2019). Zhang and Apley (2023) provides an Interpretable architecture for neural networks. We have furnished an extensive review on Shapley values in the supplementary materials, demonstrating how they can aid in understanding the importance of certain covariates.

Biv.DeepKriging can be suitable for any large-scale environmental application where high resolution spatial interpolation is a requirement.

References

- Adler, R. J. (2010). *The geometry of random fields*. SIAM.
- Agarwal, G., Y. Sun, and H. J. Wang (2021). Copula-based multiple indicator kriging for non-Gaussian random fields. *Spatial Statistics* 44, 100524.
- Apanasovich, T. V., M. G. Genton, and Y. Sun (2012). A valid Matérn class of cross-covariance functions for multivariate random fields with any number of components. *Journal of the American Statistical Association* 107(497), 180–193.
- Arain, M., R. Blair, N. Finkelstein, J. Brook, T. Sahsuvaroglu, B. Beckerman, L. Zhang, and M. Jerrett (2007). The use of wind fields in a land use regression model to predict air

- pollution concentrations for health exposure studies. *Atmospheric Environment* 41(16), 3453–3464.
- Ba, S. and V. R. Joseph (2012). Composite Gaussian process models for emulating expensive functions. *The Annals of Applied Statistics* 6(4), 1838–1860.
- Bengtsson, L. and J. Shukla (1988). Integration of space and in situ observations to study global climate change. *Bulletin of the American Meteorological Society* 69(10), 1130–1143.
- Borchani, H., G. Varando, C. Bielza, and P. Larranaga (2015). A survey on multi-output regression. *Wiley Interdisciplinary Reviews: Data Mining and Knowledge Discovery* 5(5), 216–233.
- Boucher, M.-A., L. Perreault, and F. Anctil (2009). Tools for the assessment of hydrological ensemble forecasts obtained by neural networks. *Journal of Hydroinformatics* 11(3-4), 297–307.
- Cannon, A. J. and P. H. Whitfield (2002). Downscaling recent streamflow conditions in British Columbia, Canada using ensemble neural network models. *Journal of Hydrology* 259(1-4), 136–151.
- Changyong, F., W. Hongyue, L. Naiji, C. Tian, H. Hua, L. Ying, et al. (2014). Log-transformation and its implications for data analysis. *Shanghai archives of psychiatry* 26(2), 105.

- Chen, W., Y. Li, B. J. Reich, and Y. Sun (2022). Deepkriging: Spatially dependent deep neural networks for spatial prediction. *Accepted, Statistica Sinica*, to appear.
- Cracknell, M. J. and A. M. Reading (2014). Geological mapping using remote sensing data: A comparison of five machine learning algorithms, their response to variations in the spatial distribution of training data and the use of explicit spatial information. *Computers & Geosciences* 63, 22–33.
- Cressie, N. and H.-C. Huang (1999). Classes of nonseparable, spatio-temporal stationary covariance functions. *Journal of the American Statistical Association* 94(448), 1330–1339.
- Cressie, N. and G. Johannesson (2008). Fixed rank kriging for very large spatial data sets. *Journal of the Royal Statistical Society: Series B (Statistical Methodology)* 70(1), 209–226.
- Cressie, N. A. (1993). *Statistics for spatial data*. Wiley Series in Probability and Statistics. Wiley.
- Daw, R., M. Simpson, C. K. Wikle, S. H. Holan, and J. R. Bradley (2022). An overview of univariate and multivariate Karhunen Loève Expansions in statistics. *Journal of the Indian Society for Probability and Statistics* 23, 285–326.
- De Oliveira, V., K. Fokianos, and B. Kedem (2002). Bayesian transformed Gaussian random field: A Review. *Ouyou toukeigaku* 31(3), 175–187.

- Fonseca, T. C. and M. F. Steel (2011). Non-Gaussian spatiotemporal modelling through scale mixing. *Biometrika* 98(4), 761–774.
- Fuentes, M. (2001). A high frequency kriging approach for nonstationary environmental processes. *Environmetrics: The official journal of the International Environmetrics Society* 12(5), 469–483.
- Genton, M. G. and W. Kleiber (2015). Cross-covariance functions for multivariate geostatistics. *Statistical Science* 30(2), 147–163.
- Goovaerts, P. (1998). Ordinary cokriging revisited. *Mathematical Geology* 30(1), 21–42.
- Hastie, T., R. Tibshirani, and J. Friedman (2001). The elements of statistical learning. springer series in statistics. In \therefore Springer.
- Hinton, G., N. Srivastava, and K. Swersky (2012). Neural networks for machine learning lecture 6a overview of mini-batch gradient descent. *Cited on* 14(8), 2.
- Ho, S. L., M. Xie, L. Tang, K. Xu, and T. Goh (2001). Neural network modeling with confidence bounds: a case study on the solder paste deposition process. *IEEE Transactions on Electronics Packaging Manufacturing* 24(4), 323–332.
- Jeong, D.-I. and Y.-O. Kim (2005). Rainfall-runoff models using artificial neural networks for ensemble streamflow prediction. *Hydrological Processes: An International Journal* 19(19), 3819–3835.
- Journal, A. and F. Alabert (1989). Non-Gaussian data expansion in the earth sciences. *Terra Nova* 1(2), 123–134.

- Kasiviswanathan, K. and K. Sudheer (2016). Comparison of methods used for quantifying prediction interval in artificial neural network hydrologic models. *Modeling Earth Systems and Environment* 2(1), 22.
- Khosravi, A., S. Nahavandi, D. Creighton, and A. F. Atiya (2011). Comprehensive review of neural network-based prediction intervals and new advances. *IEEE Transactions on neural networks* 22(9), 1341–1356.
- Krizhevsky, A., I. Sutskever, and G. E. Hinton (2012). Imagenet classification with deep convolutional neural networks. *Advances in neural information processing systems* 25, 1097–1105.
- LeCun, Y., Y. Bengio, and G. Hinton (2015). Deep learning. *nature* 521(7553), 436–444.
- Li, R., H. D. Bondell, and B. J. Reich (2019). Deep distribution regression.
- Li, Y., C. Wei, and T. Ma (2019). Towards explaining the regularization effect of initial large learning rate in training neural networks. *Advances in neural information processing systems* 32.
- Mao, H., R. Martin, and B. Reich (2020). Valid model-free spatial prediction.
- Merrick, L. and A. Taly (2020). The explanation game: Explaining machine learning models using shapley values. In *Machine Learning and Knowledge Extraction: 4th IFIP TC 5, TC 12, WG 8.4, WG 8.9, WG 12.9 International Cross-Domain Conference, CD-MAKE 2020, Dublin, Ireland, August 25–28, 2020, Proceedings 4*, pp. 17–38. Springer.

- Millstein, D., M. Bolinger, and R. Wiser (2022). What can surface wind observations tell us about interannual variation in wind energy output? *Wind Energy* 25, 1142–1150.
- Najafabadi, M. M., F. Villanustre, T. M. Khoshgoftaar, N. Seliya, R. Wald, and E. Muharemagic (2015). Deep learning applications and challenges in big data analytics. *Journal of big data* 2(1), 1–21.
- Neal, R. M. (2012). *Bayesian learning for neural networks*, Volume 118. Springer Science & Business Media.
- Nourani, V., N. J. Paknezhad, and H. Tanaka (2021). Prediction interval estimation methods for artificial neural network (ANN)-based modeling of the hydro-climatic processes, a Review. *Sustainability* 13(4), 1633.
- Nychka, D., S. Bandyopadhyay, D. Hammerling, F. Lindgren, and S. Sain (2015). A multiresolution Gaussian process model for the analysis of large spatial datasets. *Journal of Computational and Graphical Statistics* 24(2), 579–599.
- Nychka, D., C. Wikle, and J. A. Royle (2002). Multiresolution models for nonstationary spatial covariance functions. *Statistical Modelling* 2(4), 315–331.
- Paciorek, C. J. and M. J. Schervish (2003). Nonstationary covariance functions for Gaussian process regression. In *NIPS*, pp. 273–280. Citeseer.
- Posch, K., J. Steinbrener, and J. Pilz (2019). Variational inference to measure model uncertainty in deep neural networks.

- Reich, B. J. and M. Fuentes (2015). Spatial bayesian nonparametric methods. In *Nonparametric Bayesian Inference in Biostatistics*, pp. 347–357. Springer.
- Salvaña, M. L. O., S. Abdulah, H. Huang, H. Ltaief, Y. Sun, M. G. Genton, and D. E. Keyes (2021). High performance multivariate geospatial statistics on manycore systems. *IEEE Transactions on Parallel and Distributed Systems* 32(11), 2719–2733.
- Sanchez Gomez, M. and J. K. Lundquist (2020). The effect of wind direction shear on turbine performance in a wind farm in central iowa. *Wind Energy Science* 5(1), 125–139.
- Schmidt-Hieber, J. (2020). Nonparametric regression using deep neural networks with ReLU activation function. *The Annals of Statistics* 48(4), 1875–1897.
- Srivastav, R., K. Sudheer, and I. Chaubey (2007). A simplified approach to quantifying predictive and parametric uncertainty in artificial neural network hydrologic models. *Water Resources Research* 43, 10.
- Stein, A. and L. Corsten (1991). Universal kriging and cokriging as a regression procedure. *Biometrics* 47(2), 575–587.
- Tong, W. (2010). *Wind power generation and wind turbine design*. WIT press.
- Topalođlu, F. and H. Pehlivan (2018). Analysis of wind data, calculation of energy yield potential, and micrositing application with wasp. *Advances in Meteorology 2018*, 1687–9309.
- Vidakovic, B. (2009). *Statistical modeling by wavelets*, Volume 503. John Wiley & Sons.

- Wahba, G. (1990). *Spline models for observational data*. SIAM.
- Wang, H., Y. Guan, and B. Reich (2019). Nearest-neighbor neural networks for geostatistics. In *2019 international conference on data mining workshops (ICDMW)*, pp. 196–205. IEEE.
- Wang, Y., D. Wang, J. Zhao, and C. Zhu (2020). Wind speed spatial estimation using geostatistical kriging. In *IOP Conference Series: Earth and Environmental Science*, Volume 619, pp. 012049. IOP Publishing.
- Wikle, C. K. and A. Zammit-Mangion (2022). Statistical deep learning for spatial and spatio-temporal data.
- Xiong, Y., W. Chen, D. Apley, and X. Ding (2007). A non-stationary covariance-based kriging method for metamodelling in engineering design. *International Journal for Numerical Methods in Engineering* 71(6), 733–756.
- Xu, G. and M. G. Genton (2017). Tukey g-and-h random fields. *Journal of the American Statistical Association* 112(519), 1236–1249.
- Yip, C. M. A. (2018). *Statistical characteristics and mapping of near-surface and elevated wind resources in the Middle East*. Ph. D. thesis, KAUST.
- Zafar, M. R. and N. M. Khan (2019). Dlime: A deterministic local interpretable model-agnostic explanations approach for computer-aided diagnosis systems.
- Zammit-Mangion, A., T. L. J. Ng, Q. Vu, and M. Filippone (2021). Deep compositional spatial models. *Journal of the American Statistical Association* (0162-1459), 1–22.

Zhang, H. and A. El-Shaarawi (2010). On spatial skew-Gaussian processes and applications.

Environmetrics: The official journal of the International Environmetrics Society 21(1), 33–47.

Zhang, S. and D. W. Apley (2023). Interpretable architecture neural networks for function

visualization. *Journal of Computational and Graphical Statistics* 32, 1258 – 1271.

Zhao, J. H., Z. Y. Dong, Z. Xu, and K. P. Wong (2008). A statistical approach for interval

forecasting of the electricity price. *IEEE Transactions on Power Systems* 23(2), 267–276.

SUPPLEMENTARY MATERIAL

Exploratory analysis of the wind field data: Wind field estimates play a fundamental role in many applications, such as power generation (Tong, 2010), hydrological modelling (Topaloglu and Pehlivan, 2018; Millstein et al., 2022) and monitoring and predicting weather patterns and global climate (Arain et al., 2007; Bengtsson and Shukla, 1988). So it is of great interest to get accurate interpolation of wind fields at unobserved locations to exploit the huge potential of wind data for different fields. Wind is generally quantified as a bivariate variable with two components, U and V , where U is the zonal velocity, i.e., the component of the horizontal wind towards east and V is the meridional velocity, i.e., the component of the horizontal wind towards north. The wind speed at any location can then be defined as $\sqrt{U^2 + V^2}$.

We analyze wind at $5km \times 5km$ spatial resolution for January, 2009 (7) from a Weather Research and Forecasting (WRF) model simulation on the $[30^\circ E, 65^\circ E] \times [5^\circ N, 35^\circ N]$ region of Earth (Yip, 2018) which spans the Middle East. Figure 7 shows non-stationarity, e.g., the surface is more rough over land than water. The scatter plot in Figure 8 shows a nonlinear relation between the two components. Furthermore, the marginal density plots (Figure 9) of the individual components shows that the data has heavy tails implying non-Gaussianity. Hence, the explanatory analysis provides evidence towards a multivariate non-stationary covariance and non-Gaussian distribution. Traditional Kriging methodologies cannot accommodate these features.

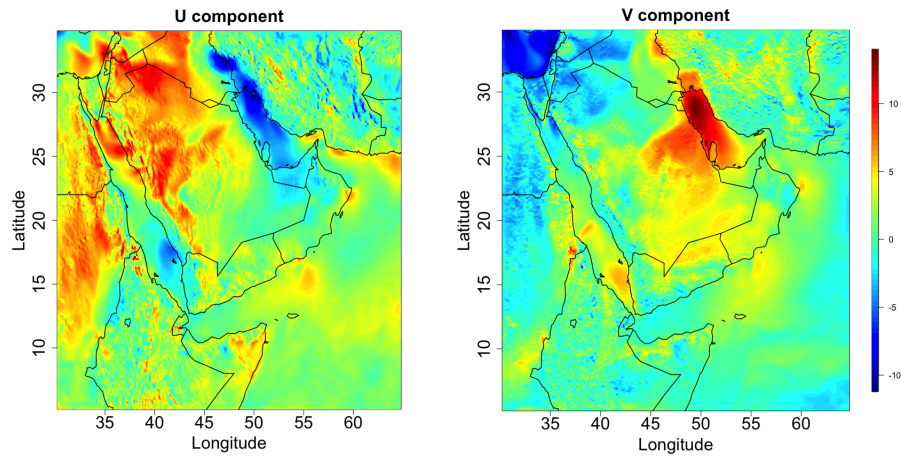


Figure 7: Visualization of the U and V components of the wind field over the Middle East region

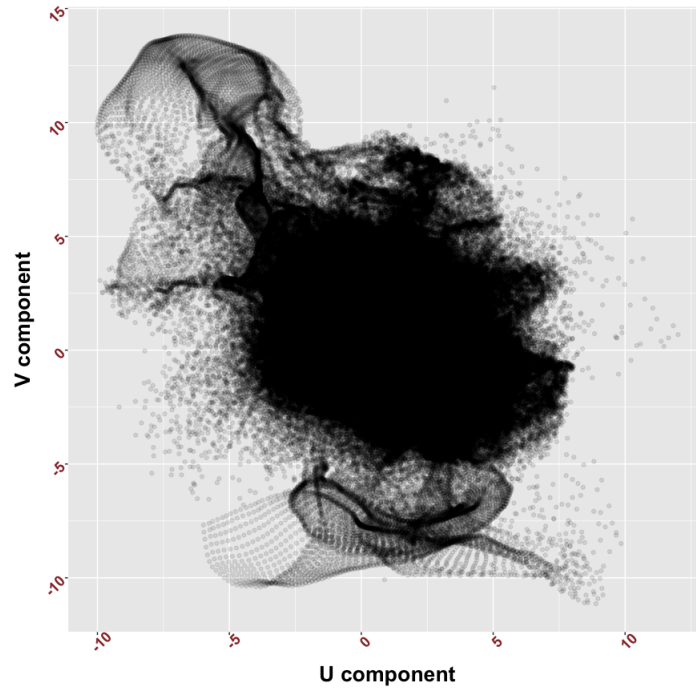


Figure 8: Scatter plot of the U and V components of the Middle Eastern wind field

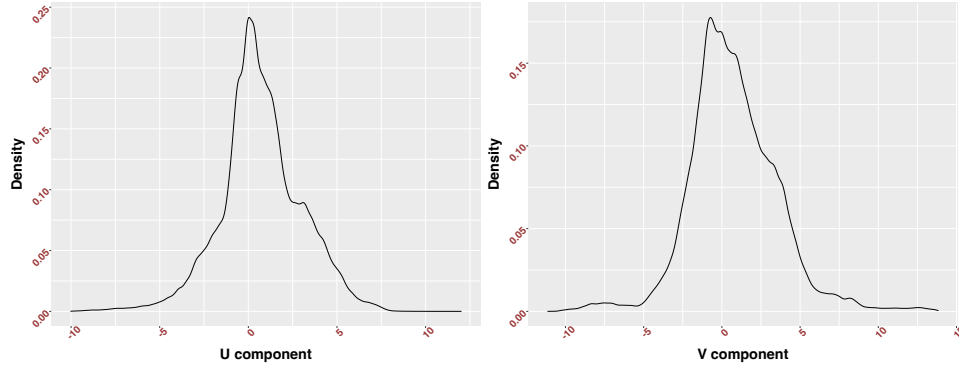


Figure 9: Sample marginal density plots of the U and V components of the Middle Eastern wind data

Simulations details and additional results: In this section, we provide details regarding comparisons involving Gaussian Processes (GP). We generate two-dimensional stationary Gaussian processes utilizing the parsimonious Matérn covariance function. The simulated data is derived from a zero-mean GP with bivariate Matérn covariance characterized by a cross-correlation coefficient of $\rho = 0.8$, variances $\sigma_1 = 0.89$ and $\sigma_2 = 1.3$, smoothness parameters $\nu_1 = \nu_2 = 0.8$, and range parameters $\alpha_1 = 0.2$ and $\alpha_2 = 0.4$.

We generate 100 replicates employing the aforementioned parameter configuration on 1200 irregularly spaced locations spanning $[0, 1] \times [0, 1]$. For training purposes, we utilize 1080 points, reserving the remainder for testing. The results can be seen in Table 4.

Although the nonlinear structure of **Biv.DeepKriging** captures more specific features from data we still need to validate that our proposal for extending the univariate DeepKriging (Chen et al., 2022) to Bivariate scenario improves the prediction results by exploiting the dependence within the variables. To do this, we compare our pro-

posed model with the univariate DeepKriging model predictions. We compute the average **MSPE** independently for each variable over 100 replicates. Table 4 shows that the Bivariate DeepKriging provides better performance in the prediction error than the independent univariate DeepKriging (**Indep.DeepKriging**) fitted with the same network architecture.

Table 4: Comparison of **MSPE** for both the variables and its standard error (**SE**) for stationary Gaussian processes.

Simulation type	Models	MSPE ₁	SE ₁	MSPE ₂	SE ₂
Gaussian	CoKriging.Matérn _{true}	0.23	0.91 ($\times 10^{-4}$)	0.21	0.93 ($\times 10^{-4}$)
	Indep.DeepKriging	0.25	1.21 ($\times 10^{-4}$)	0.26	2.32 ($\times 10^{-4}$)
	Biv.DeepKriging	0.24	1.33 ($\times 10^{-4}$)	0.24	1.17 ($\times 10^{-4}$)

Nonstationary simulation: The simulation focuses on bivariate data with non-stationary feature. To do so, we followed several computer examples (Ba and Joseph, 2012; Xiong et al., 2007) to generate the non-stationary data by deterministic functions which gives non-stationarity in the data. We simulate $\mathbf{Y}(\mathbf{s})$ with $\boldsymbol{\mu}(\mathbf{s}) = \{\mu_1(\mathbf{s}), \mu_2(\mathbf{s})\}$ where

$$\begin{aligned}\mu_1(\mathbf{s}) &= \sin \{5(\bar{s} - 0.9)\} \cos \{25(\bar{s} - 0.9)^4\} + \frac{(\bar{s} - 0.9)}{2} \\ \mu_2(\mathbf{s}) &= \sin \{2(\bar{s} - 0.9)\} \cos \{30(\bar{s} - 0.9)^4\} - \frac{(\bar{s} - 0.9)}{2}\end{aligned}$$

$\bar{s} = \frac{x+y}{2}$, where $\mathbf{s} = \{x, y\}$ and $\boldsymbol{\gamma}(\mathbf{s})$ follows bivariate **GP** with variance variances $\sigma_1 = 0.01$ and $\sigma_2 = 0.01$ and the remaining covariance parameters are same as the Gaussian simulation parameterization . The graphical plot of the data can be viewed in Figure 10.

From Figure 10, it is evident that the dataset exhibits roughness in the lower-left region, while appearing comparatively smoother towards the top. This observation

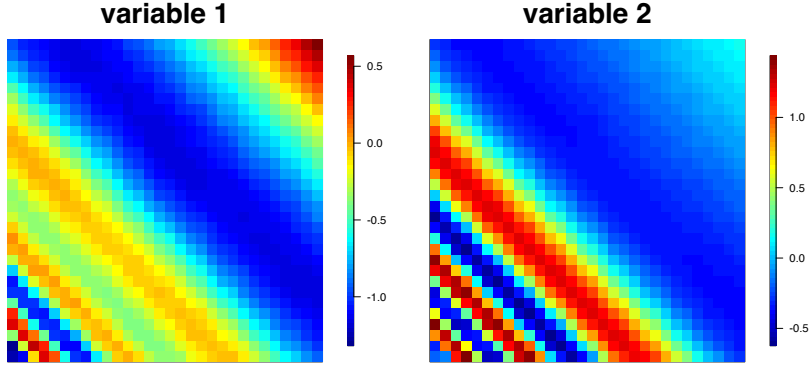


Figure 10: Visualization of the simulated nonstationary data.

suggests that employing the same model structure across the entire region may not be appropriate. The CoKriging model structure overlooks this spatial nonstationarity, whereas bivariate DeepKriging demonstrates adaptability to such variations, emerging as a more flexible modeling option. To further substantiate this claim, we computed the absolute error deviation for each test location individually and compared the results with the **CoKriging.Matérn** model, which is the second best-performing model after **Biv.DeepKriging**. In Figure 11, it can be observed that the absolute error remains minimal for both models over the smoother surface. However, towards the lower-left region, the absolute error significantly increases for **CoKriging.Matérn** compared to **Biv.DeepKriging**. This discrepancy implies that the CoKriging model fails to capture the spatial nonstationarity adequately, whereas bivariate DeepKriging demonstrates superior performance in this aspect.

Details on Neural Network Training: We employed the following deep neural network architecture for modeling:

- We utilized 3 layers of basis functions with $K = 4, 16, 25$ respectively, resulting

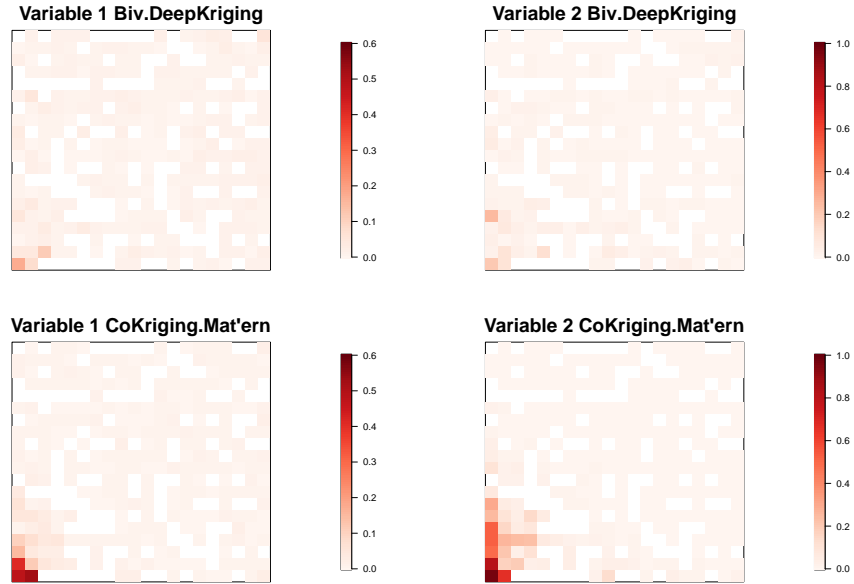


Figure 11: Comparison of absolute deviation of predictions from the truth between **Biv.DeepKriging** and **CoKriging.Mat'ern**. We computed these deviations for the test locations for both the variables.

in a total of 45 basis functions for all our simulation scenarios.

- The neural network comprises 8 layers with $M_1 = M_2 = M_3 = M_4 = M_5 = 100$ for the first 5 layers, and $M_6 = M_7 = 50$, $M_8 = 2$ nodes in the final three layers.
- Weight matrices were initialized by sampling from a uniform distribution.
- The training dataset was split into a 90%-10% ratio for training and validation on each epoch, and the model showing the best performance on validation was saved.
- Hyperparameters such as learning rate (Li et al., 2019), number of epochs, and batch size were chosen based on validation. A step-by-step approach to choosing these hyperparameters is explained below:
 - Initially, a certain number of layers L and nodes per layer M were chosen

based on prior experience, considering the nature of the dataset, which is spatial data in this case, and building upon previous work [Chen et al. \(2022\)](#).

- Once L and M were determined, attention shifted to other hyperparameters.
 - A high value for the number of epochs was set initially, and the learning rate was adjusted. If optimization did not occur due to a high learning rate causing the training loss to plateau, the learning rate was decreased gradually.
 - After fixing the learning rate, different batch sizes were tested to observe their effect on the training loss.
 - Based on observations, the number of epochs required for complete optimization became apparent.
 - If results were unsatisfactory, L and M were adjusted iteratively. Overfitting was monitored by examining the training and validation loss.
- Through iterative experiments, optimal hyperparameters were selected. For non-Gaussian simulations, we used a learning rate of 0.001, batch size of 512, and a total of 1250 epochs. For nonstationary experiments, a learning rate of 0.001, batch size of 256, and 1500 epochs were chosen.

Performance of Biv.DeepKriging conditioned on number of layers: We conducted

a comparative study involving three different DNN architectures for both non-Gaussian simulations and real data. Table 5 gives a comprehensive overview on the performance of **Biv.DeepKriging** in varied architectures. We denoted the number of layers for each model by the subscript added to it. It can be seen from the MSPEs that

Biv.DeepKriging $_{L=2}$ underfits the data, **Biv.DeepKriging** $_{L=15}$ overfits it. The optimum number of layers $L = 8$ provides best result here.

Table 5: Comparison of average **MSPE** for both the variables for different scenarios.

data type	Model	MSPE $_1$	MSPE $_2$
non-Gaussian	Biv.DeepKriging $_{L=2}$	35.94	48.70
	Biv.DeepKriging $_{L=8}$	32.71	23.83
	Biv.DeepKriging $_{L=15}$	32.88	24.33
real data	Biv.DeepKriging $_{L=2}$	0.732	0.875
	Biv.DeepKriging $_{L=8}$	0.394	0.392
	Biv.DeepKriging $_{L=15}$	0.433	0.413

The Shapley value: The Shapley value of a feature value represents its contribution to the payout, weighted and summed over all possible feature value combinations:

$$\psi_j(\text{val}) = \sum_{S \subseteq \{1, \dots, p\} \setminus \{j\}} \frac{|S|!(p - |S| - 1)!}{p!} (\text{val}(S \cup \{j\}) - \text{val}(S))$$

where S is a subset of the features used in the model, \mathbf{x} is the vector of feature values of the instance to be explained, and p is the number of features. $\text{val}_x(S)$ is the prediction for feature values in set S that are marginalized over features not included in set S . From this point onward, we denote $\hat{f}_{NN_1}(\cdot)$ as $\hat{f}(\cdot)$:

$$\text{val}_x(S) = \int \hat{f}(x_1, \dots, x_p) d\mathbb{P}_{x \notin S} - E_X(\hat{f}(X))$$

where X is a random variable of the feature.

Multiple integrations are performed for each feature not contained in S . For example, for a model with five features x_1, x_2, x_3, x_4 , and x_5 , and evaluating the prediction for the coalition S consisting of feature values x_1 and x_3 :

$$\text{val}_x(S) = \text{val}_x(\{1, 3\}) = \int_{\mathbb{R}} \int_{\mathbb{R}} \hat{f}(x_1, X_2, x_3, X_4, X_5) d\mathbb{P}_{X_2 X_4 X_5} - E_X(\hat{f}(X))$$

The Shapley value is the only attribution method that satisfies the properties of Efficiency, Symmetry, Dummy, and Additivity, which together can be considered a definition of a fair payout.

Estimating the Shapley Value

To calculate the exact Shapley value, all possible coalitions (sets) of feature values must be evaluated with and without the j -th feature. However, for a large number of features, the exact solution becomes problematic due to the exponentially increasing number of possible coalitions. An approximation with Monte Carlo sampling can be written as:

$$\hat{\psi}_j = \frac{1}{M} \sum_{m=1}^M (\hat{f}(x_{+j}^m) - \hat{f}(x_{-j}^m))$$

where $\hat{f}(x_{+j}^m)$ is the prediction for \mathbf{x} with a random number of feature values replaced by feature values from a random data point \mathbf{z} , except for the respective value of feature j . The \mathbf{x} -vector x_{-j}^m is almost identical to x_{+j}^m , except the value x_j^m is also taken from the sampled \mathbf{z} . Each of these M new instances is a combination of two instances, akin to "Frankenstein's Monster."

The following algorithm outlines the approximate Shapley estimation for a single feature value:

Algorithm: Approximate Shapley estimation for a single feature value

- **Output:** Shapley value for the value of the j -th feature
- **Required:** Number of iterations M , instance of interest \mathbf{x} , feature index j , data matrix \mathbf{X} , and machine learning model f
- For all $m = 1, \dots, M$:
 - Draw random instance \mathbf{z} from the data matrix \mathbf{X}
 - Choose a random permutation o of the feature values
 - Order instance \mathbf{x} : $\mathbf{x}_o = (x_{(1)}, \dots, x_{(j)}, \dots, x_{(p)})$

- Order instance \mathbf{z} : $\mathbf{z}_o = (z_{(1)}, \dots, z_{(j)}, \dots, z_{(p)})$
- Construct two new instances:
 - * With j : $\mathbf{x}_{+j} = (x_{(1)}, \dots, x_{(j-1)}, x_{(j)}, z_{(j+1)}, \dots, z_{(p)})$
 - * Without j : $\mathbf{x}_{-j} = (x_{(1)}, \dots, x_{(j-1)}, z_{(j)}, z_{(j+1)}, \dots, z_{(p)})$
- Compute marginal contribution: $\psi_j^m = \hat{f}(\mathbf{x}_{+j}) - \hat{f}(\mathbf{x}_{-j})$
- Compute Shapley value as the average: $\psi_j(\mathbf{x}) = \frac{1}{M} \sum_{m=1}^M \psi_j^m$

The procedure must be repeated for each feature to obtain all Shapley values.

We utilize the Shapley value method to interpret the covariates associated with the non-Gaussian scenario. Several examples are provided below. Figure 12 illustrates the partial dependence of covariate 5 on variable 1, while Figure 13 demonstrates the contribution of each covariate on variable 1 for the test location \mathbf{s}_{35} .

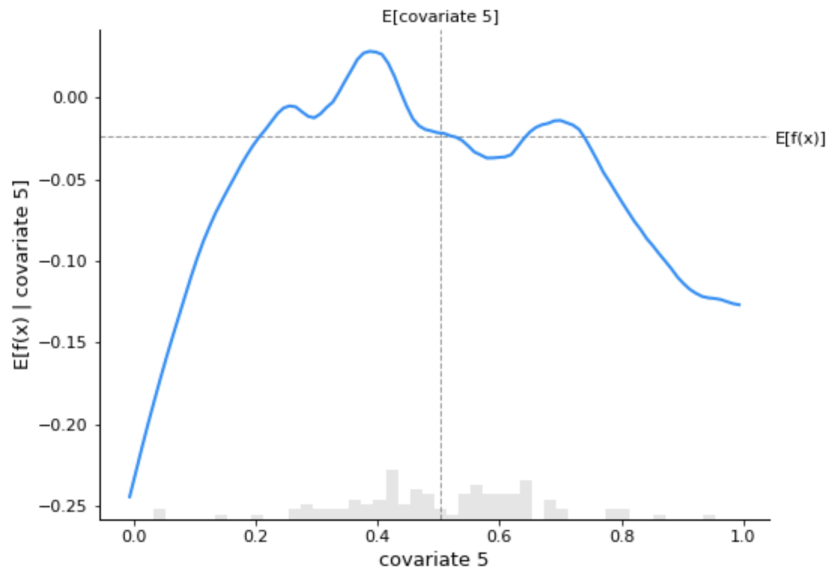


Figure 12: Visualization of the dependence of Covariate 5 on the response.

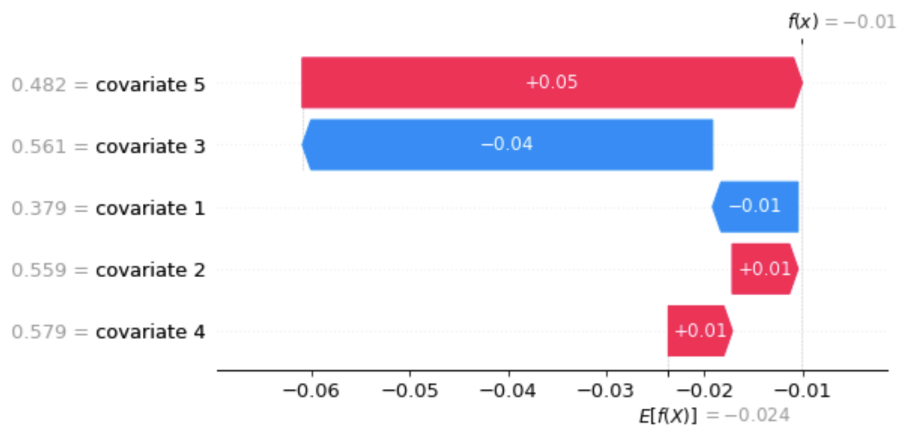


Figure 13: A comparative study of all covariate contributions on the response at the test location s_{35} .